Virtual Inductance and DC Boosting Control Based Low Voltage Ride-Through Method for Doubly-Fed Variable-Speed Pumped Hydro Storage Units

Xin Li, *Member, IEEE*, Yingjie Chen, Weike Yu, Longquan Li, Pengfei Yao, Jianxi Lan, Jian Ai, and Wu Chen, *Senior Member, IEEE*

***Abstract*—This article proposes a novel low-voltage ride-through (LVRT) control strategy for doubly-fed variable-speed pumped hydro storage (VS-PHS) units. Unlike conventional LVRT approaches for doubly-fed induction generators (DFIGs) that mainly rely on crowbar circuits or virtual inductance control, the proposed strategy combines rotor-side virtual inductance with dc-link voltage boosting, fully leveraging the tolerance of pumped hydro units to elevated dc-link voltages during pumping-mode self-startup. In this way, it overcomes the inherent limitations of single virtual inductance control and extends the applicable range of virtual inductance control. A real-time digital simulation platform of a 300 MW VS-PHS unit is established to validate the method. Simulation results demonstrate that the proposed strategy not only suppresses rotor overcurrent more effectively than conventional demagnetization control but also provides reactive power support during faults, offering clear advantages over existing DFIG LVRT strategies. It can still operate safely and stably under severe voltage drops of up to 80% . This ensures secure and stable operation in both generating and pumping modes, across a wide speed range and under varying fault severities.**

***Index Terms*—DC-link voltage, doubly-fed induction generator (DFIG), low voltage ride through (LVRT), real-time digital simulation (RTDS), virtual inductance control.**

I. Introduction

DUE to the randomness, volatility, and intermittency of new energy power generation, energy storage systems are emerging as critical infrastructure for integrating renewable energy sources and optimizing grid stability by managing energy supply-demand imbalances [1].

The increasing penetration of renewable energy sources, such as wind and solar, is accelerating this trend, while also imposing more stringent requirements on fault-ride-through capability [2]. In particular, low-voltage ride-through (LVRT) has become a critical requirement for large-capacity grid-connected equipment in modern power systems [3].

Compared to energy storage methods such as batteries, flywheels, superconductors, and supercapacitors, pumped hydro storage is an effective large-capacity energy storage method, offering advantages such as large storage capacity, fast response speed, and high conversion efficiency [4]. The existing pumped hydro storage facilities predominantly employ conventional synchronous-speed units. However, the fixed-frequency operation restricts the accuracy and efficiency of the power regulation.

Compared with conventional fixed-speed systems, variable-speed pumped hydro storage (VS-PHS) units utilizing doubly-fed induction generator (DFIG) technology can achieve variable-speed constant-frequency with agile and wide-range power regulation capability [5], [6]. The use of a small-capacity rotor-side converter (RSC) with DFIG offers a cost-effective solution suitable for high-power applications, reducing converter size while enabling high efficiency and flexibility [7]. Currently, two 300 MW units in Fengning Power Station in China that adopts doubly-fed VS-PHS units have been put into operation for the first time, providing technical assurance and engineering demonstration for the large-scale development and construction in the future.

However, as stator of the DFIG is directly connected to the grid, the doubly-fed VS-PHS units is very sensitive to grid voltage fluctuations. When a grid voltage drop occurs, the stator terminal voltage drops abruptly. However, due to the inductive nature of the stator, the stator flux cannot change instantaneously, resulting in a transient dc component. This transient flux induces a significant electromotive force (EMF) in the rotor circuit [8]. The EMF is then transmitted through the rotor windings to the input of the RSC, potentially endangering the safety of the converter's IGBT modules. Therefore, a certain level of LVRT capability is necessary.

The existing LVRT strategies for DFIG-based systems can generally be classified into hardware-based protection methods and software-based control strategies. Among hardware approaches [9], [10], the most widely adopted and cost-effective solution is the deployment of a Crowbar circuit on the

---

Received 21 April 2025; revised 29 July 2025 and 25 September 2025; accepted 9 October 2025. Date of publication 20 October 2025; date of current version 19 January 2026. This work was supported in part by the National Natural Science Foundation of China under Grant 52307196, in part by the Natural Science Foundation of Jiangsu Province under Grant BK20230850, in part by the Jiangsu Provincial Key Laboratory of Smart Grid Technology and Equipment under Grant 4216002201, and in part by the Zhishan Young Scholar Support Program of Southeast University under Grant 3216002505A2. Recommended for publication by Associate Editor M. Molinas. *(Corresponding author: Jian Ai.)*

Xin Li, Yingjie Chen, Weike Yu, Longquan Li, Pengfei Yao, Jianxi Lan, and Wu Chen are with the School of Electrical Engineering, Southeast University, Nanjing 210096, China (e-mail: li-xin@seu.edu.cn; 220243073@seu.edu.cn; 220243087@seu.edu.cn; yao-pengfei@seu.edu.cn; jfwang@seu.edu.cn; chenwu@seu.edu.cn).

Jian Ai is with Jiangnan University, Wuxi 214122, China (e-mail: jianai0204@jiangnan.edu.cn).

Color versions of one or more figures in this article are available at https://doi.org/10.1109/TPEL.2025.3623779.

Digital Object Identifier 10.1109/TPEL.2025.3623779

rotor side. When a grid voltage fault is detected, the Crowbar circuit is triggered, and the RSC is disabled from pulse emission, thereby diverting the fault current through the Crowbar resistor to protect the RSC from overcurrent damage. Extensive studies have been conducted on optimizing the switching logic [11], resistor design [12], and topological configurations [13] of Crowbar circuits to improve their fault response characteristics.

However, the main limitation of hardware Crowbar solutions lies in the fact that once the RSC is deactivated, the unit becomes entirely uncontrollable, thereby losing its key advantage of flexible power regulation and dynamic grid support. Moreover, although alternative hardware approaches such as dc bus chopper circuits have been proposed to suppress dc-link voltage overshoots during faults, these methods do not address the issue of rotor-side fault currents. As a result, many practical implementations still rely on hybrid configurations that combine Crowbar circuits with chopper circuits, which adds system complexity while still failing to fully exploit the control potential of the RSC during LVRT events.

These limitations underscore the need for more advanced active control-based LVRT strategies, particularly for DFIG-based VS-PHS units, where maintaining control flexibility across both operating modes is essential.

In terms of software-based protection, existing LVRT strategies for DFIG systems can generally be categorized into the following three main approaches [14]:

1) feedforward control with induced EMF compensation;
2) enhanced disturbance rejection through advanced current loop design;
3) demagnetizing current injection techniques.

In study [15], a feedforward compensation strategy was proposed based on grid voltage, stator flux, and stator excitation current variations. Both stator voltage-oriented control and stator flux-oriented control methods were analyzed, offering broad applicability across different grid scenarios. However, this approach suffers from inherent limitations such as excessive demagnetizing currents, pronounced torque pulsations, and the added complexity of requiring stator flux observation and phase-sequence decoupling. To improve current loop performance, various advanced control structures have been proposed in studies [16], [17], [18], and [19], including sliding mode control, hysteresis control, internal model control, and fuzzy logic control, which aim to enhance the current loop's disturbance rejection and reduce current tracking errors. While these approaches improve rotor current dynamics, they do not fully address key challenges such as flux decay time constants and large rotor-induced EMF during deep voltage sags. Demagnetization control [20] is considered a classical LVRT technique, wherein the transient component of the stator flux is extracted using a flux observer, and the rotor current is actively controlled to track both free and negative-sequence components of the stator flux, thereby achieving a demagnetizing effect. However, this method is sensitive to flux observer accuracy and introduces greater system complexity due to the required real-time flux estimation. In study [21], a scaled stator current tracking control approach was proposed, wherein the rotor current is constrained to track the stator current within a certain range using an optimized tracking coefficient, thus ensuring that rotor current remains within the RSC's safe operating range. However, this method overlooks the requirement to accelerate stator flux decay, resulting in a prolonged transient recovery process during fault clearing. In studies [22] and [23], a virtual damping control strategy was developed to accelerate stator flux transient decay by effectively increasing the equivalent damping of the flux dynamics, thereby suppressing rotor current oscillations. Nevertheless, this method demands an excessively high rotor voltage, which introduces the risk of converter saturation or even loss of control under severe grid fault conditions. In studies [24] and [25], a cascade converter-based solution that can effectively enhance both LVRT and HVRT performance of the DFIG system was proposed. The cascade converter can operate under both voltage sags and swells, improving system damping and maintaining fault ride-through capability with much lower converter ratings compared to other hardware-based solutions.

Although significant progress has been made in software-based LVRT control for DFIG systems, most existing studies have focused primarily on doubly-fed wind turbines, while research on doubly-fed VS-PHS units remains relatively limited. Although both systems utilize DFIG technology and therefore share certain similarities in LVRT control, VS-PHS units exhibit distinct operational characteristics compared to wind turbines. In particular, they must alternate between generating and pumping modes, with the direction of power flow in the rotor-side converter dynamically reversing according to the operating mode. This introduces unique control challenges that are rarely encountered in wind turbine applications [26].

Moreover, during grid voltage faults, the LVRT controller of a VS-PHS unit must not only ensure effective fault ride-through capability in both operating modes but also enable smooth transitions and recovery between them. However, most existing LVRT solutions for pumped storage systems still rely heavily on hardware-based Crowbar circuits, which suffer from limited control flexibility and cannot deliver optimal dynamic performance across the entire dual-mode operating range [27]. It is worth noting that VS-PHS units possess certain unique features in pumping mode—such as self-start capability—that can be leveraged to develop more effective LVRT strategies. Therefore, exploring targeted LVRT control methods that account for the fundamental differences between VS-PHS units and wind turbines is of great research significance.

This article addresses the LVRT control problem of VS-PHS units. The main contributions are as follows.

1) A systematic analysis of the interaction between the proposed virtual inductance control and rotor-side dynamics, clarifying the influence of rotor current and flux linkage during grid faults.
2) An investigation of stability margins under different dc-link voltage limits.
3) An analytical derivation of the safe range of virtual inductance, considering both rotor-side dynamics and converter capability constraints.

Compared with other control strategies, the proposed method in this article has the following advantages.

1) Compared with conventional crowbar methods, the proposed method protects the converter by limiting rotor overcurrents while maintaining flexible controllability of

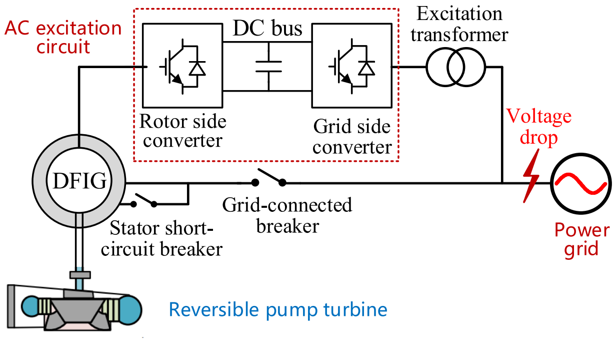

Fig. 1. Diagram of the structure of doubly-fed VS-PHS units.

the unit. In addition, it can provide reactive power support to the grid, which facilitates voltage recovery.

2) Compared to demagnetization control, the proposed method limits rotor-side overcurrents more effectively with better use of the power characteristics during faults.
3) Compared with approaches using only virtual impedance or virtual inductance, the proposed strategy incorporates dc-link voltage boosting and fully exploits the inherent power imbalance during faults. This enables a wider slip range and a higher voltage ride-through capability.

The remainder of this article is organized as follows: Section II discusses the operating characteristics of VS-PHS units, with emphasis on the differences between pumping and generating modes. Section III analyzes the variations of rotor EMF and current during voltage sags. Section IV introduces the principle of virtual inductance control, outlines its challenges, and proposes an improved dc-link voltage control strategy tailored to the wide speed range of VS-PHS units. Section V presents the simulation results, and Section VI concludes this article.

II. OPERATION MODE OF DOUBLY-FED VARIABLE-SPEED PUMPED HYDRO STORAGE UNIT

The structure of the doubly-fed VS-PHS unit is shown in Fig. 1. It mainly consists of a doubly-fed motor, an ac excitation circuit, an excitation transformer, and a reversible pump-turbine. The rotor side is connected to the grid through the ac excitation circuit composed of back-to-back inverters and the excitation transformer, while the stator side is directly connected to the grid. Therefore, energy is exchanged between the stator, rotor, and the grid.

In generating mode, the stator winding is initially disconnected from the grid, placing the DFIG in a no-load state. The hydraulic turbine and its governor system then drive the rotor to accelerate. Once the rotor speed reaches a predetermined synchronization threshold and the excitation converter is ready, the excitation system is activated. The grid side converter (GSC) regulates the dc-link voltage, while the RSC injects excitation current into the rotor, gradually building up the stator voltage.

When the stator output voltage of the generator matches the grid voltage in magnitude, phase, and frequency, the synchronization conditions are satisfied, and the grid-connected breaker is closed to complete the grid connection. After connected with grid, the system enters generating control mode, where the RSC regulates both active and reactive power exchange between the DFIG and the grid, and the GSC continuously maintains dc-link voltage stability.

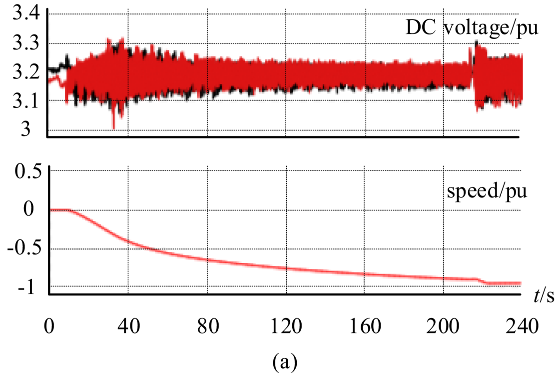

(a)

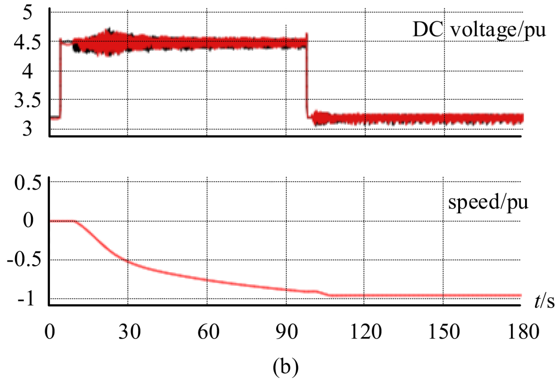

(b)

Fig. 2. Simulation waveforms of the self-startup process. (a) DC-link voltage is 6400 V. (b) DC-link voltage is 9000 V.

In pumping mode, there is no external mechanical drive, so the rotor must be started via electromagnetic torque. The stator is initially short-circuited to provide electrical damping, while the ac excitation system applies an excitation voltage of increasing amplitude and frequency to the rotor windings. To accelerate the heavy rotating mass of the machine more efficiently, the GSC is controlled to increase the dc-link voltage, thereby expanding the voltage margin of the RSC and enabling it to deliver stronger excitation current to the rotor. For example, in the studied VSPS unit, the dc-link voltage is normally maintained at 6400 V, but during self-startup, it is boosted to 9000 V—approximately 1.4 times the nominal level. As the rotor begins to accelerate under the effect of electromagnetic torque, it smoothly builds up speed. When it reaches the reference value near synchronous speed, the RSC pulse output is temporarily blocked, and the stator short-circuit switch is opened, placing the stator in open-circuit condition. The RSC then adjusts the rotor excitation to further increase the stator terminal voltage. Once the stator voltage matches the grid in magnitude, phase, and frequency, synchronization is performed by closing the grid connection switch.

After synchronization, the system enters pumping operation mode, where the RSC regulates the active and reactive power exchange with the grid, and the GSC continues to stabilize the dc-link voltage.

Fig. 2 illustrates the self-startup waveforms of the variable-speed pumped storage unit under different conditions. Since the

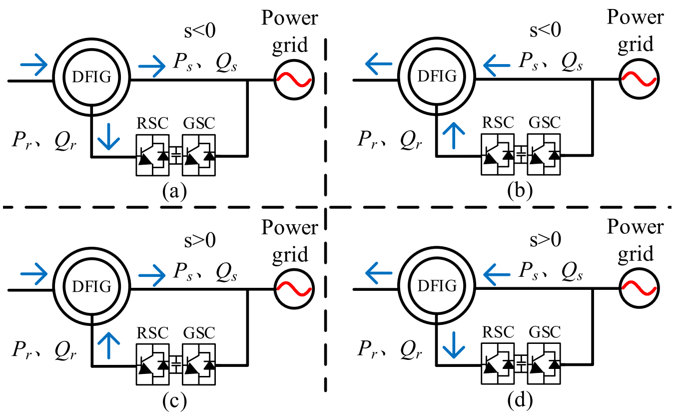

Fig. 3. Grid-connected operation mode. (a) Generating mode, supersynchronous operation. (b) Pumping mode, supersynchronous operation. (c) generating mode, subsynchronous operation. (d) Pumping mode, subsynchronous operation.

dc-link voltage is divided across upper and lower capacitors, the voltage is $U_{\mathrm{dc}}/2$, and the speed reference is set to –0.9 p.u. (as the machine rotates in reverse during pumping mode, the speed is negative). Fig. 2(a) shows the case with a 6400 V dc-link voltage, while Fig. 2(b) corresponds to a 9000 V dc-link voltage. It can be observed that the self-startup time is approximately 220 s at 6400 V, whereas it is reduced to around 100 s at 9000 V. This indicates that increasing the dc-link voltage significantly shortens the self-startup time. Therefore, in practical design, a certain voltage margin is typically reserved in the dc-link to enhance the RSC's ability to supply excitation current, and hardware parameters are usually specified based on this higher voltage level. This design feature distinguishes variable-speed pumped storage units from wind turbines and also provides an important inspiration for the LVRT control strategy proposed in this study.

After grid synchronization, the system operates in four states as shown in Fig. 3, where s denotes the slip of the machine, P_{s} and Q_{s} represent the stator-side active and reactive power, and P_{r} and Q_{r} represent the rotor-side active and reactive power.

III. TRANSIENT CHARACTERISTICS OF ROTOR SIDE EQUIVALENT CIRCUIT DURING GRID VOLTAGE DROPS

The expression for the rotor-side voltage and current can be expressed as follows [28]:

$$\boldsymbol{u}_{\mathrm{r}} = \frac{L_{\mathrm{m}}}{L_{\mathrm{s}}}\frac{\mathrm{d}\boldsymbol{\psi}_{\mathrm{s}}}{\mathrm{dt}} + \left[R_{\mathrm{r}} + \sigma L_{\mathrm{r}}\frac{\mathrm{d}}{\mathrm{dt}}\right]\boldsymbol{i}_{\mathrm{r}} \tag{1}$$

where $\boldsymbol{u}$ represents the voltage vector; $\boldsymbol{i}$ denotes the current vector; $\boldsymbol{\psi}$ signifies the flux linkage vector; the subscripts "s" and "r" refer to the stator and rotor, respectively; L_{s} and L_{r} are the self-inductances of the stator and rotor windings, respectively; L_{m} is the mutual inductance between the stator and rotor windings; R_{s} and R_{r} are the resistances of the stator and rotor windings, respectively; and σ is leakage coefficient and $\sigma = 1\text{-}L_{\mathrm{m}}^2/(L_{\mathrm{s}}L_{\mathrm{r}})$.

The rotor voltage in (1) can be divided into two parts. The first part is the induced EMF caused by the stator flux linkage. When the rotor is open-circuited, this term also represents the rotor open-circuit voltage, hence denoted as $\boldsymbol{u}_{\mathrm{ro}}$. The second part is the voltage drop across the rotor impedance.

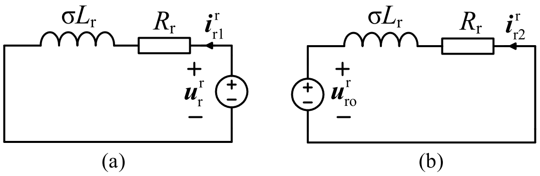

Fig. 4. Rotor side equivalent circuit during faults. (a) Equivalent subcircuit under the RSC voltage excitation. (b) Equivalent subcircuit under the rotor open-circuit voltage excitation.

Rotor open-circuit voltage $\boldsymbol{u}_{\mathrm{ro}}$ reflects the electromagnetic coupling relationship between the stator and rotor. During grid voltage fault, the rotor current, dc-link voltage, and electromagnetic torque of the doubly-fed VS-PHS unit is primarily influenced by $\boldsymbol{u}_{\mathrm{ro}}$. Therefore, it is necessary to first analyze the variation of the rotor open-circuit voltage.

Assuming a three-phase symmetrical fault occurs in the grid voltage at $t = 0$, and given that the stator of the doubly-fed VS-PHS unit is directly connected to the grid, the analytical expression for the stator flux linkage after the fault can be obtained as follows [28]:

$$\boldsymbol{\psi}_{\mathrm{s}} = \boldsymbol{\psi}_{\mathrm{sf}} + \boldsymbol{\psi}_{\mathrm{sn}} = \frac{(1-h)\,U_{\mathrm{s}}}{j\omega_{\mathrm{s}}}\mathrm{e}^{j\omega_{\mathrm{s}}t} + \frac{hU_{\mathrm{s}}}{j\omega_{\mathrm{s}}}\mathrm{e}^{-\frac{t}{\tau_{\mathrm{s}}}} \tag{2}$$

where the stator flux linkage consists of a rotating ac component $\boldsymbol{\psi}_{\mathrm{sf}}$ and a decaying dc component $\boldsymbol{\psi}_{\mathrm{sn}}$; h represents the voltage drop degree, where $0<h<1$; U_{s} is the amplitude of stator voltage; ω_{s} is the frequency of stator voltage; j represents the imaginary part; and τ_{s} is the stator time constant and $\tau_{\mathrm{s}} = L_{\mathrm{s}}/R_{\mathrm{s}}$.

Substituting (2) into (1) and transforming it into the rotor reference frame yields the analytical expression for the rotor open-circuit voltage

$$\boldsymbol{u}_{\mathrm{ro}}^{\mathrm{r}} = \frac{L_{\mathrm{m}}}{L_{\mathrm{s}}}\left[s\,(1-h)\,U_{\mathrm{s}}e^{js\omega_{\mathrm{s}}t} - (1-s)\,hU_{\mathrm{s}}e^{-\left(\frac{1}{\tau_{\mathrm{s}}}+j\omega_{\mathrm{r}}\right)t}\right] \tag{3}$$

where ω_{r} is the frequency of rotor voltage; and s represents slip rate.

The rotor current is influenced by two components: the open-circuit voltage $\boldsymbol{u}_{\mathrm{ro}}^{\mathrm{r}}$ and the converter output voltage $\boldsymbol{u}_{\mathrm{r}}^{\mathrm{r}}$. To derive the analytical expression of the rotor current, the superposition principle is applied, resulting in two equivalent subcircuits of the rotor-side during the fault period, as shown in Fig. 4. As per Fig. 4, the following can be derived:

$$\begin{cases} \boldsymbol{i}_{\mathrm{r1}}^{\mathrm{r}} = \frac{\boldsymbol{u}_{\mathrm{r}}^{\mathrm{r}}}{R_{\mathrm{r}}+j\omega_{\mathrm{r}}\sigma L_{\mathrm{r}}} \\ \boldsymbol{i}_{\mathrm{r2}}^{\mathrm{r}} = -\frac{\boldsymbol{u}_{\mathrm{ro}}^{\mathrm{r}}}{R_{\mathrm{r}}+j\omega_{\mathrm{r}}\sigma L_{\mathrm{r}}} \end{cases} \tag{4}$$

$$\boldsymbol{i}_{\mathrm{r}}^{\mathrm{r}} = \boldsymbol{i}_{\mathrm{r1}}^{\mathrm{r}} + \boldsymbol{i}_{\mathrm{r2}}^{\mathrm{r}}. \tag{5}$$

Here, $\boldsymbol{i}_{\mathrm{r1}}^{\mathrm{r}}$ represents the rotor current component influenced by the RSC voltage, and $\boldsymbol{i}_{\mathrm{r2}}^{\mathrm{r}}$ denotes the rotor current component influenced by the rotor open-circuit voltage.

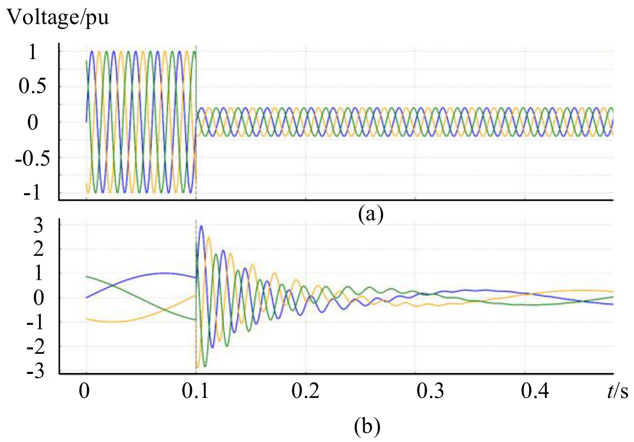

(a)

(b)

Fig. 5. Stator voltage and rotor open-circuit voltage waveforms before and after 80% voltage drop happens at 0.1 s. (a) Stator voltage. (b) Rotor open-circuit voltage.

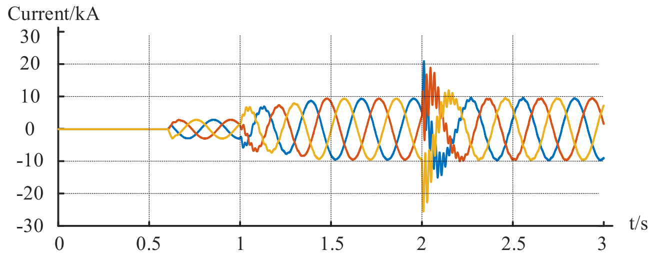

Fig. 6. Rotor current waveforms when 80% voltage drop happens at 2 s.

By solving the above equations comprehensively, $\boldsymbol{i}_{\mathrm{r}}^{\mathrm{r}}$ can be solved as follows:

$$\boldsymbol{i}_{\mathrm{r}}^{\mathrm{r}}=\frac{U_{\mathrm{r}}e^{j\omega_{\mathrm{r}}t}-\frac{L_{\mathrm{m}}}{L_{\mathrm{s}}}\left(s\left(1-h\right)U_{\mathrm{s}}e^{js\omega_{\mathrm{s}}t}-\left(1-s\right)hU_{\mathrm{s}}e^{-\left(\frac{1}{\tau_{\mathrm{s}}}+j\omega_{\mathrm{r}}\right)t}\right)}{R_{\mathrm{r}}+j\omega_{\mathrm{r}}\sigma L_{\mathrm{r}}} \tag{6}$$

During the LVRT process, the main challenge lies in the fact that the stator flux linkage induces a significant EMF on the rotor side, namely the rotor open-circuit voltage $\boldsymbol{u}_{\mathrm{ro}}^{\mathrm{r}}$, which in turn affects the rotor current $\boldsymbol{i}_{\mathrm{r}}^{\mathrm{r}}$.

The waveform of the rotor open-circuit voltage after the voltage drop can be plotted based on (3). As illustrated in the equivalent circuit, the rotor current $\boldsymbol{i}_{\mathrm{r}}^{\mathrm{r}}$ is driven by the difference between the induced open-circuit voltage $\boldsymbol{u}_{\mathrm{ro}}^{\mathrm{r}}$ and the terminal voltage $\boldsymbol{u}_{\mathrm{r}}^{\mathrm{r}}$, with the total rotor-side impedance consisting of σL_r, R_r, and the virtual impedance Z_{RSC}. When a grid voltage drop occurs, the stator voltage drops rapidly, while the magnetic flux in the stator cannot change instantaneously due to the presence of the stator-side leakage and mutual inductances. This results in a sharp increase in the rotor-side induced voltage $\boldsymbol{u}_{\mathrm{ro}}^{\mathrm{r}}$, as shown in the waveform in Fig. 5, which exhibits a transient overshoot up to approximately 3 p.u.

Fig. 6 presents the simulation waveform of the rotor current for a DFIG operating in generating mode under an 80% voltage drop. The relevant simulation parameters are listed in Table I.

TABLE I
PARAMETERS OF 300 MW DOUBLY FED VS-PHS UNIT

Parameters	Values
Rated power	300MW
Rated voltage	18kV
Rated frequency	50Hz
Rated speed	428rpm
Maximum slip rate s	0.07
Stator resistance R_{s}	0.001341pu
Stator leakage X_{ls}	0.1208pu
Rotor resistance R_{r}	0.001405pu
Rotor leakage X_{lr}	0.1868pu
Excitation reactance X_{m}	2.383pu
Impedance base value	0.9257Ω
Pole pairs p	7
maximum current I_{rmax}	20kA
maximum voltage U_{rmax}	10kV

As visualized in Fig. 5, the rotor current transient at 80% voltage drop reaches nearly three times the nominal operating current.

Under this sudden increase of $\boldsymbol{u}_{\mathrm{ro}}^{\mathrm{r}}$, the voltage across the rotor impedance path significantly increases. Since the impedance remains unchanged during this short transient periods, Ohm's law dictates that the rotor current must increase proportionally. This explains why the rotor current reaches several times its pre-fault value at the moment of voltage drops.

This current may significantly exceed the converter's rated capacity. Without additional protective schemes, the RSC faces the risk of overcurrent. Should protective relaying systems detect this, the unit may be forced to disconnect from the grid to protect the RSC. However, with the escalating power ratings of modern converter units, directly disconnecting the unit during a grid fault could further exacerbate the grid fault.

Therefore, it is necessary to incorporate an LVRT control strategy into the RSC control system.

IV. ANALYSIS OF LOW-VOLTAGE RIDE-THROUGH CONTROL STRATEGY

The voltage drop across the rotor impedance is denoted as $\boldsymbol{u}_{\mathrm{r1}}^{\mathrm{r}}$, with the equivalent output impedance of the RSC represented by Z_{RSC}. Incorporates these parameters the equivalent circuit on the rotor side is shown in Fig. 7, and the rotor loop satisfies the following:

$$\begin{cases}\boldsymbol{u}_{\mathrm{ro}}^{\mathrm{r}}+\boldsymbol{u}_{\mathrm{r1}}^{\mathrm{r}}=\boldsymbol{u}_{\mathrm{r}}^{\mathrm{r}}\\ \boldsymbol{u}_{\mathrm{r1}}^{\mathrm{r}}=\left(R_{\mathrm{r}}+j\omega_{\mathrm{r}}\sigma L_{\mathrm{r}}\right)\boldsymbol{i}_{\mathrm{r}}^{\mathrm{r}}.\\ \boldsymbol{u}_{\mathrm{r}}^{\mathrm{r}}=-Z_{RSC}\boldsymbol{i}_{\mathrm{r}}^{\mathrm{r}\prime}\end{cases} \tag{7}$$

Given the resistance in the rotor circuit is negligible compared to the reactive impedance, it can be approximated that the angle θ_1 between $\boldsymbol{u}_{\mathrm{r1}}^{\mathrm{r}}$ and $\boldsymbol{i}_{\mathrm{r}}^{\mathrm{r}}$ is 90°. Let the angle between $\boldsymbol{u}_{\mathrm{r}}^{\mathrm{r}}$ and $\boldsymbol{i}_{\mathrm{r}}^{\mathrm{r}}$ be θ_2, then the voltage relationship within the rotor loop satisfies the

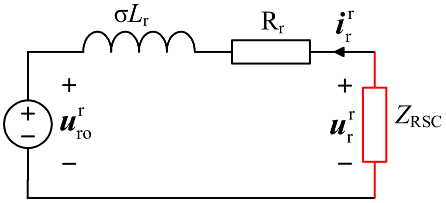

Fig. 7. Rotor side equivalent circuit.

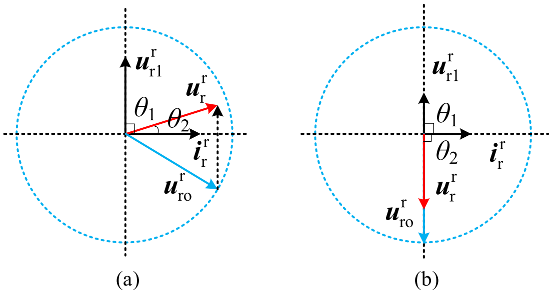

(a) (b)

Fig. 8. Rotor voltage phasor diagram of the rotor circuit. (a) Arbitrary equivalent impedance conditions. (b) Inductive equivalent impedance conditions.

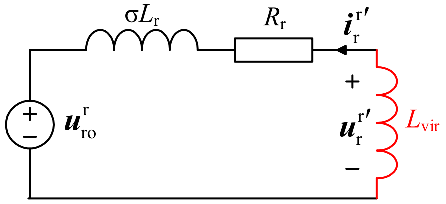

Fig. 9. Rotor side equivalent circuit under virtual inductance control.

phasor diagram in Fig. 8. As per (3), the open-circuit voltage $\boldsymbol{u}_\mathrm{ro}^\mathrm{r}$ depends solely on the voltage drop level, slip ratio, and inherent motor parameters, so the magnitude of $\boldsymbol{u}_\mathrm{ro}^\mathrm{r}$ can be considered constant. Consequently, when the RSC terminal presents varying impedance characteristics, the rotor current magnitude $\boldsymbol{i}_\mathrm{r}^\mathrm{r}$ will exhibit corresponding variations for a specified rotor voltage . Fig. 8(a) shows the rotor voltage phasor diagram of the rotor circuit when it exhibits arbitrary impedance characteristics, and the vector relationship shows that the magnitude of the rotor current $\boldsymbol{i}_\mathrm{r}^\mathrm{r}$ is related to θ_2.

As shown in Fig. 8(b), when the phase angles satisfy $\theta_1 = \theta_2$ the rotor voltage vector $\boldsymbol{u}_\mathrm{r}^\mathrm{r}$ aligns with the angle of the open-circuit rotor voltage $\boldsymbol{u}_\mathrm{ro}^\mathrm{r}$. Under this condition, minimizing the rotor current magnitude $|\boldsymbol{i}_\mathrm{r}^\mathrm{r}|$ for a given $\boldsymbol{u}_\mathrm{r}^\mathrm{r}$ is achieved by aligning $\boldsymbol{i}_\mathrm{r}^\mathrm{r}$ in the same direction as the voltage drop across the virtual inductance, which lags behind $\boldsymbol{u}_\mathrm{ro}^\mathrm{r}$ by 90°. In this case, the net voltage $\boldsymbol{u}_\mathrm{r}^\mathrm{r} - \boldsymbol{u}_\mathrm{ro}^\mathrm{r}$ is purely inductive, and its magnitude is minimized when the current vector points in this lagging direction. This alignment ensures that for a fixed output voltage vector $\boldsymbol{u}_\mathrm{r}^\mathrm{r}$, the resulting current magnitude is as small as possible, thereby reducing rotor overcurrent risk during grid faults.

The transient equivalent circuit incorporating the equivalent inductance L_vir is illustrated in Fig. 9. During this dynamic phase, the rotor current is denoted as $\boldsymbol{i}_\mathrm{r}^{\mathrm{r}\prime}$, and the port voltage output by the rotor-side converter $\boldsymbol{u}_\mathrm{r}^{\mathrm{r}\prime}$ is exactly the voltage drop across the equivalent inductance, which satisfies the following:

$$-j\omega_\mathrm{r} L_\mathrm{vir} \boldsymbol{i}_\mathrm{r}^{\mathrm{r}\prime} = R_\mathrm{r} \boldsymbol{i}_\mathrm{r}^{\mathrm{r}\prime} + j\omega_\mathrm{r} \sigma L_\mathrm{r} \boldsymbol{i}_\mathrm{r}^{\mathrm{r}\prime} + \boldsymbol{u}_\mathrm{ro}^\mathrm{r} \tag{8}$$

$$\boldsymbol{u}_\mathrm{r}^{\mathrm{r}\prime} = -\, j\omega_\mathrm{r} L_\mathrm{vir} \boldsymbol{i}_\mathrm{r}^{\mathrm{r}\prime} \tag{9}$$

And (5), (6) become

$$\begin{cases} \boldsymbol{i}_\mathrm{r1}^{\mathrm{r}}{}' = \frac{\boldsymbol{u}_\mathrm{r}^{\mathrm{r}\prime}}{R_\mathrm{r} + j\omega_\mathrm{r}\sigma L_\mathrm{r}} \\ \boldsymbol{i}_\mathrm{r2}^{\mathrm{r}}{}' = -\frac{\boldsymbol{u}_\mathrm{ro}^\mathrm{r}}{R_\mathrm{r} + j\omega_\mathrm{r}\sigma L_\mathrm{r}} \end{cases} \tag{10}$$

$$\boldsymbol{i}_\mathrm{r}^{\mathrm{r}\prime} = \boldsymbol{i}_\mathrm{r1}^{\mathrm{r}}{}' + \boldsymbol{i}_\mathrm{r2}^{\mathrm{r}}{}' \tag{11}$$

On the basis of (8)–(11), the following equations are derived:

$$\boldsymbol{i}_\mathrm{r}^{\mathrm{r}\prime} = -\frac{\boldsymbol{u}_\mathrm{ro}^\mathrm{r}}{R_\mathrm{r} + j\omega_\mathrm{r}\left(\sigma L_\mathrm{r} + L_\mathrm{vir}\right)} \tag{12}$$

$$\boldsymbol{u}_\mathrm{r}^{\mathrm{r}\prime} = j\omega_\mathrm{r} L_\mathrm{vir} \frac{\boldsymbol{u}_\mathrm{ro}^\mathrm{r}}{R_\mathrm{r} + j\omega_\mathrm{r}\left(\sigma L_\mathrm{r} + L_\mathrm{vir}\right)}. \tag{13}$$

Through analysis of (12) and (13), it reveals that the greater the value of L_vir is, the smaller $\boldsymbol{i}_\mathrm{r}^{\mathrm{r}\prime}$ becomes, and the larger $\boldsymbol{u}_\mathrm{r}^{\mathrm{r}\prime}$ becomes. Therefore, increasing the equivalent inductance L_vir enhances the suppression of the rotor current, but the voltage that the RSC needs to output also increases. Due to the limited capacity of the converter, both voltage and current must operate within strict operational boundaries, which requires the equivalent inductance value to be judiciously constrained.

Considering the maximum allowable current and the maximum output voltage of the RSC are I_rmax and U_rmax, the rotor current must satisfy the subsequent operational constraint:

$$\left|\boldsymbol{i}_\mathrm{r}^{\mathrm{r}\prime}\right| = \frac{\left|\boldsymbol{u}_\mathrm{ro}^\mathrm{r}\right|}{\sqrt{R_\mathrm{r}^2 + \omega_\mathrm{r}^2\left(\sigma L_\mathrm{r} + L_\mathrm{vir}\right)^2}} \leq I_\mathrm{r\,max}. \tag{14}$$

Solving (14) yields the following expression:

$$L_\mathrm{vir} \geq \frac{\sqrt{\left|\boldsymbol{u}_\mathrm{ro}^\mathrm{r}\right|^2 - \left(I_\mathrm{r\,max} R_\mathrm{r}\right)^2}}{I_\mathrm{r\,max}\omega_\mathrm{r}} - \sigma L_\mathrm{r}. \tag{15}$$

The rotor voltage satisfies the following:

$$\left|\boldsymbol{u}_\mathrm{r}^{\mathrm{r}\prime}\right| = \frac{\omega_\mathrm{r} L_\mathrm{vir}\left|\boldsymbol{u}_\mathrm{ro}^\mathrm{r}\right|}{\sqrt{R_\mathrm{r}^2 + \omega_\mathrm{r}^2\left(\sigma L_\mathrm{r} + L_\mathrm{vir}\right)^2}} \leq U_\mathrm{r\,max}. \tag{16}$$

Solving (16), we have the following:

$$L_\mathrm{vir} \leq \frac{\sqrt{\left(U_\mathrm{r\,max} R_\mathrm{r}\right)^2} + \omega_\mathrm{r}\sigma L_\mathrm{r}}{\omega_\mathrm{r}\sqrt{\left|\boldsymbol{u}_\mathrm{ro}^\mathrm{r}\right|^2 - U_\mathrm{r\,max}^2}}. \tag{17}$$

Therefore, the equivalent virtual inductance must simultaneously satisfy the constraints given by (15) and (17).

From (15) and (17), it can be seen that L_vir is related to the motor's intrinsic parameters, the voltage and current limits of the RSC, and the magnitude of the rotor open-circuit voltage. The magnitude of the rotor open-circuit voltage, as shown in (3), varies with the slip rate *s* and the voltage drop degree h. The larger the slip rate *s* or the deeper the voltage drop degree h, the greater the magnitude of the rotor open-circuit voltage. Figs. 10

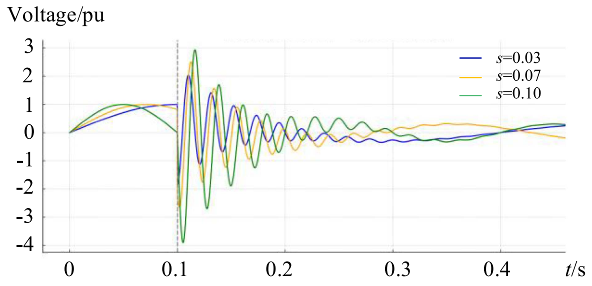

Fig. 10. Rotor open-circuit voltage under different slip rates, $h = 0.8$.

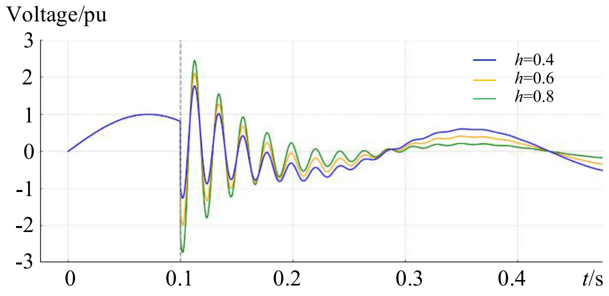

Fig. 11. Rotor open-circuit voltage under different voltage drop degrees, $s = 0.07$.

and 11 show the waveforms of the rotor open-circuit voltage under different slip rates and voltage drop degrees, respectively.

To achieve high efficiency, doubly-fed VS-PHS units typically necessities flexible adjustments of the rotational speed based on different operating conditions. It should be noted that when a high degree of voltage drop fault occurs with a large slip rate, the induced electromotive force on the rotor side (i.e., $\boldsymbol{u}_{\mathrm{ro}}$) becomes large. In this case, it may no longer be possible to use (15) and (17) to determine a valid range for L_{vir}.

The magnitude of $\boldsymbol{u}_{\mathrm{ro}}^{\mathrm{r}}$ exhibits a certain degree of randomness under different operating conditions. If $\boldsymbol{u}_{\mathrm{ro}}^{\mathrm{r}}$ is large, it may lead to the failure of the virtual inductance control strategy. From (15) and (17), it can be seen that among the variables affecting the value of L_{vir}, we cannot easily change the motor's intrinsic parameters and the maximum current allowed by the RSC, I_{rmax}. In the back-to-back converter excitation system, the output voltage of the RSC is limited by the dc-link voltage, which means that U_{rmax} in (17) is constrained by the dc-link voltage. Under normal operating conditions, the dc-link voltage in the excitation circuit of the unit studied in this article is 6400 V. However, considering the characteristics of the doubly-fed VS-PHS unit itself, the unit inherently requires an elevated dc-link voltage during self-startup in pumping mode. When the dc-link voltage increases, the output voltage capability of the RSC also improves. If this approach is applied during LVRT, it can effectively increase U_{rmax}. Therefore, based on (17), an increase in U_{rmax} can expand the upper limit of the L_{vir} value range, meaning that the unit can handle higher rotor open-circuit voltage, thereby preventing overcurrent on the rotor side.

Under this premise, assuming that the dc-link voltage output controlled by the GSC during low voltage ride-through is increased by a factor of k, then U_{rmax} will also increase by a factor of k. The value of k depends on the control range of the dc-link voltage considered during the self-starting process when designing doubly-fed VS-PHS units. In this article, k is taken as 1.4. At this point, (17) becomes as follows:

$$L_{\mathrm{vir}} \leq \frac{\sqrt{\left(kU_{\mathrm{r\,max}}R_{\mathrm{r}}\right)^2 + \omega_{\mathrm{r}}\sigma L_{\mathrm{r}}}}{\omega_{\mathrm{r}}\sqrt{\left|\boldsymbol{u}_{\mathrm{ro}}^{\mathrm{r}}\right|^2 - k^2U_{\mathrm{r\,max}}^2}}. \tag{18}$$

In (18), the increase of U_{rmax} lead to the increase of numerator, and the decrease of denominator, resulting in an increase in the upper limit of L_{vir}. This expands the application range of the virtual inductance control, allowing it to handle faults under more severe voltage drops or operating conditions with larger slip rates.

From a theoretical perspective, increasing the dc-link voltage is feasible for two main reasons. On one hand, the doubly-fed VS-PHS units inherently require an elevated dc-link voltage during self-startup in pumping mode—and this elevated state must be sustained for a relatively long duration (approximately 100 s)—increasing the dc-link voltage during LVRT will not impose any additional stress on the hardware components.

On the other hand, when a fault occurs, the rotor-side induced electromotive force rises sharply, leading to an increase in rotor-side power. During this period, the stator is unable to effectively transmit power to the grid. Due to this power imbalance, the anti-parallel diodes in the RSC conduct, transferring the excess energy to the dc-link and causing the dc-link voltage to rise. During this process, if the GSC is simultaneously controlled to actively absorb power from the grid and raise the dc-link voltage, energy will flow into the dc-link from both the rotor and grid sides, facilitating a rapid voltage increase. Meanwhile, the conduction path provided by the anti-parallel diodes of the RSC allows for the release of unbalanced power on the rotor side.

The overall control block diagram of the proposed system is illustrated in Fig. 12. The proposed strategy can effectively suppress rotor overcurrent during voltage sag conditions, thereby ensuring continuous grid connection of the generating unit. In addition, it increases the maximum rotor voltage U_{rmax}, which improves the control margin. Simultaneously, by providing an effective energy release path, it helps mitigate rotor-side power imbalance, thus facilitating a successful low-voltage ride-through process.

V. EXPERIMENTAL VERIFICATION

To validate the correctness and feasibility of the proposed control strategy, a simulation model of a doubly-fed VS-PHS unit was constructed based on the RTDS simulation platform. The motor has a rated power of 300 MW, a stator rated voltage of 18 kV, and a rated speed of 428 r/min. During the simulation, the motor slip rate is controlled at 0.07. The relevant parameters of the unit are listed in Table I.

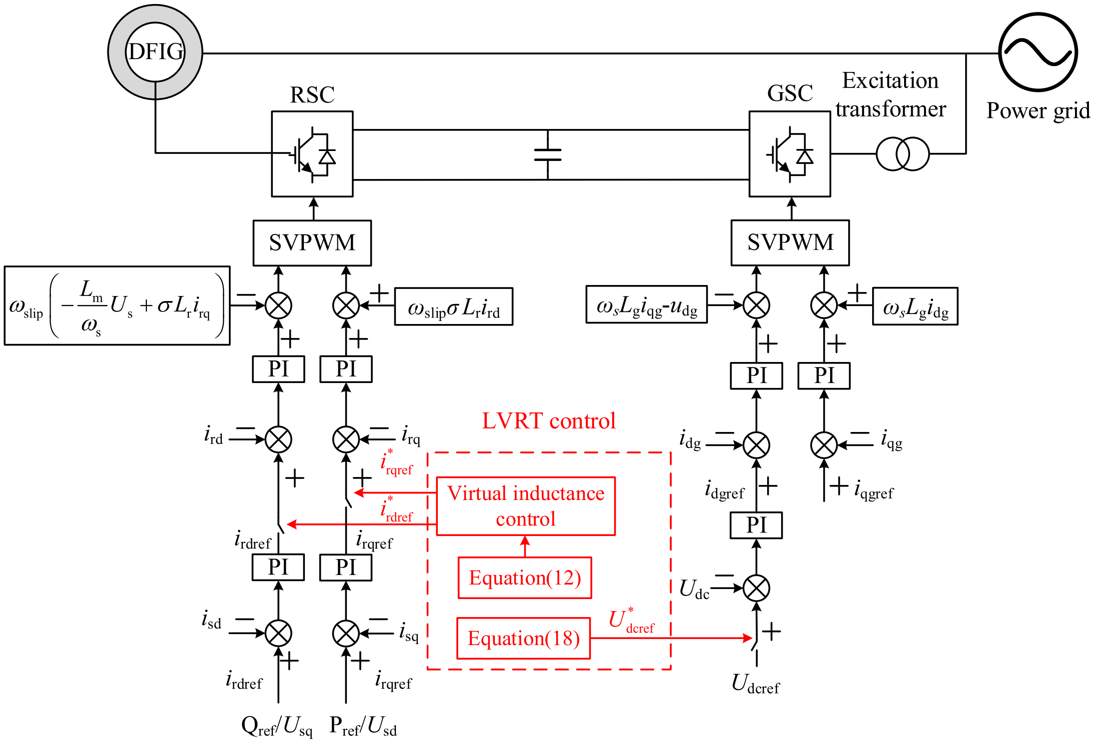

Fig. 12. System control block diagram of the proposed control strategy.

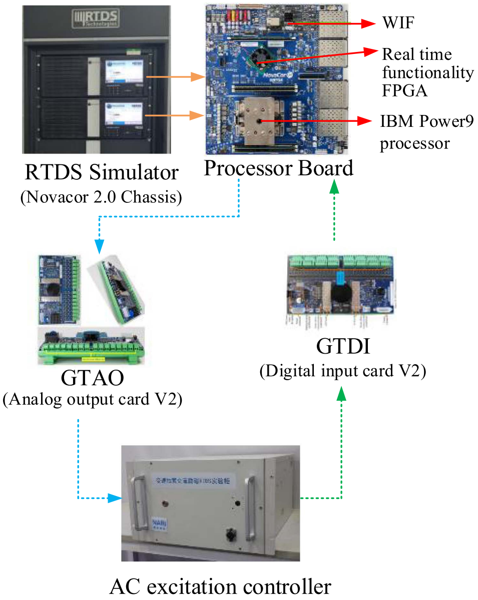

Fig. 13. RTDS simulation platform of doubly-fed VS-PHS unit.

Fig. 13 illustrates the hardware architecture of the simulation platform. The RTDS Simulator is designed to perform real-time electromagnetic transient simulation. It is composed of multiple processor boards, which consist of WIF (a green or red light indicates this status as good or bad), real time functionality FPGA and IBM power9 processor. The RTDS Simulator is connected with ac excitation control cabinets by GTAO (analog output card) and GTDI (digital input card) boards. The analog signals such as voltage and current are transmitted to the ac excitation control cabinet through the GTAO board, and the pulsewidth modulation pulse signal generated by the ac excitation control cabinet is received through the GIDI board.

In the RTDS simulation, the primary focus was on the voltage and current constrains on the rotor side during transient processes. The maximum allowable current on the rotor side is 20 kA, and the maximum allowable voltage is 10 kV. Therefore, certain simplifications were applied to the simulation model: the grid was simplified as an ideal model, neglecting harmonics and unbalanced components; the cooling, temperature rise, temperature-dependent variations, magnetic saturation, and long-term aging effects of the converter and machine were not considered, the hydraulic turbine was simplified as a transfer-function model governing rotor speed. These simplifications do not affect the transient simulation results.

Figs. 14–16 have a comparison of the RTDS simulation waveforms by a commonly used LVRT control method and the proposed LVRT method employing virtual inductance and dc boosting control. Comprehensive comparative analyses are performed for both control strategies under generating and pumping modes, with 80% voltage drops. The voltage drop occurs at $t = 0.9$ s and recovers at $t = 1.525$ s, lasting for 0.625 s. In this study, the rotor current limit of the unit under normal operation is 9 kA (RMS). Therefore, during reactive power support, the entire rotor current capacity is utilized for reactive power injection. Under fault conditions, the rotor current peak limit is 20 kA. If the fault current exceeds 20 kA, the converter's internal protection mechanisms will be triggered. From top to bottom, the simulation results shown in the figure are the stator

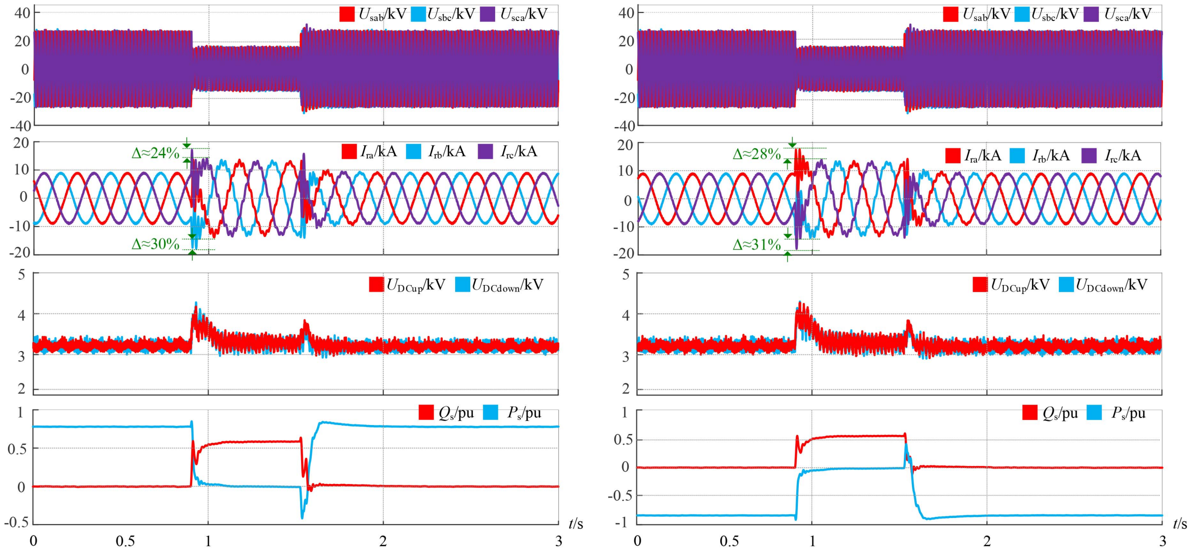

(a) (b)

Fig. 14. Demagnetization control [18], voltage drop by 80% , slip rate 0.07. (a) Generating mode. (b) Pumping mode.

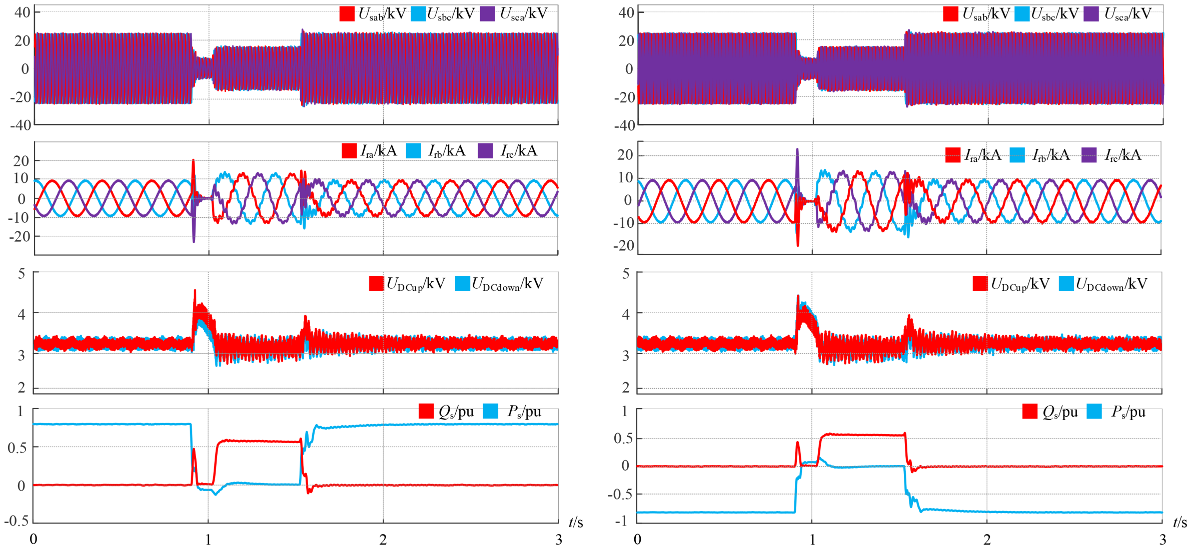

(a) (b)

Fig. 15. Virtual inductance control without DC boosting, voltage drop by 80% , slip rate 0.07. (a) Generating mode. (b) Pumping mode.

three-phase line voltages, rotor three-phase currents, upper and lower dc-link voltages, and the active and reactive power output from the stator.

Fig. 14 shows the results under demagnetization control [18], where Fig. 14(a) corresponds to the generating mode and Fig. 14(b) to the pumping mode. In generating mode, when the fault occurs, the peak rotor current exceeds the normal value by approximately 24% and 30% . In pumping mode, the peak rotor current exceeds the normal value by approximately 28% and 31% during the fault. This indicates that demagnetization control has a certain suppressive effect on the rotor current during faults.

Fig. 15 presents the simulation results when only the virtual inductance control is applied, without the dc boosting control. In this case, the virtual inductance is set to approximately $3L_{\mathrm{lr}}$. As shown in the figure, in both generating and pumping modes, the rotor current peak exceeds 20 kA shortly after the fault occurs. This triggers the protection mechanism of the converter, causing the converter pulses to be blocked temporarily for self-protection. Under such severe voltage drop and large slip conditions, the virtual inductance control fails. The root cause is that the induced EMF on the rotor side becomes excessively high, making the upper limit of the available virtual inductance smaller than the lower limit. As

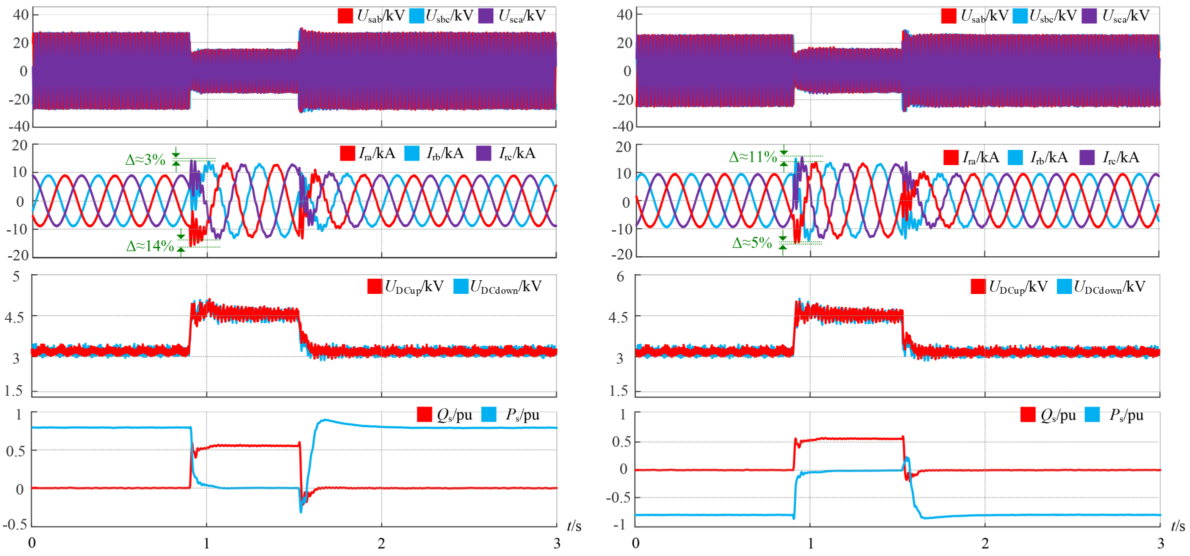

(a) (b)

Fig. 16. Virtual inductance control with DC boosting, voltage drop by 80% , slip rate 0.07. (a) Generating mode. (b) Pumping mode.

a result, the rotor overcurrent cannot be suppressed regardless of the virtual inductance value. During the pulse blocking period, the converter ceases operation, and the machine is unable to provide reactive power support to the grid, leading to a temporary stagnation in stator terminal voltage recovery. Once the converter resumes operation, the machine begins supplying some reactive power, and the terminal voltage rises accordingly.

Both Figs. 14 and 15 show that, regardless of the control method used, the dc-link voltage exhibits a significant upward trend at the moment of the fault if left uncontrolled, and it returns to normal after a short period. This is because the large induced EMF on the rotor side after the fault causes the anti-parallel diode of the RSC to conduct, allowing the unbalanced power to flow into the dc link through the diode.

Fig. 16 illustrates the simulation results when both virtual inductance and dc boosting control strategies are applied, with the virtual inductance again set to approximately $3\,L_{\mathrm{lr}}$. In generating mode, the rotor current peaks exceed the normal values by only about 3% and 14% , while in pumping mode, they exceed by around 11% and 5% . Compared to demagnetization control, the rotor current peaks are significantly more suppressed, indicating that the proposed strategy is more effective in limiting overcurrent. Meanwhile, thanks to the bidirectional power flow provided by the RSC anti-parallel diode and the GSC, the dc-link voltage can rise rapidly and remain stable. A higher dc-link voltage enhances the RSC's voltage output capability, allowing the virtual inductance control strategy to handle more severe fault conditions.

The simulation results clearly demonstrate that the proposed LVRT control strategy outperforms conventional demagnetization control in suppressing rotor overcurrent. Therefore, this control strategy significantly improves the LVRT capability of the unit, validating the effectiveness and correctness of the proposed method.

VI. CONCLUSION

This article investigates LVRT control strategies for doubly-fed VS-PHS units and proposes an improved method that combines rotor-side virtual inductance with dc-link voltage boosting control. By exploiting the unique tolerance of VS-PHS units in pumping mode and the inherent power imbalance during faults, the proposed strategy reduces rotor transient current peaks by approximately 15% in both generating and pumping modes compared with conventional demagnetization control. Moreover, by incorporating dc-link voltage boosting, the method extends the operational slip range to 0.07 and enhances voltage ride-through capability up to 80% , surpassing approaches that rely solely on virtual impedance or inductance. In contrast to conventional crowbar-based LVRT protection, the proposed method preserves machine controllability, enables converter-supplied excitation, and delivers reactive power support to the grid, thereby improving voltage stability. The effectiveness of the strategy is validated through the RTDS platform for the VS-PHS system.

REFERENCES

[1] J. Zhang et al., "A capacity-expandable cascaded multilevel energy storage system based on laminated power modules," *IEEE Trans. Power Electron.*, vol. 40, pp. 5265–5278, Apr. 2025.

[2] M. G. Taul, X. Wang, P. Davari, and F. Blaabjerg, "Robust fault ride through of converter-based generation during severe faults with phase jumps," *IEEE Trans. Ind. Appl.*, vol. 56, no. 1, pp. 570–583, Jan./Feb. 2020.

[3] R. Hiremath and T. Moger, "Comparative analysis of different controllers for enhancing the LVRT of DFIG system," in *Proc. 9th Int. Renewable Sustain. Energy Conf.*, 2021, pp. 1–5.

[4] A. Joseph and T. R. Chelliah, "A review of power electronic converters for variable speed pumped storage plants: Configurations, operational challenges, and future scopes," *IEEE J. Emerg. Sel. Topics Power Electron.*, vol. 6, no. 1, pp. 103–119, Mar. 2018.

[5] A. Joseph, K. Desingu, R. R. Semwal, T. R. Chelliah, and D. Khare, "Dynamic performance of pumping mode of 250 MW variable speed hydro-generating unit subjected to power and control circuit faults," *IEEE Trans. Energy Convers.*, vol. 33, no. 1, pp. 430–441, Mar. 2018.

[6] Y. Chen, C. Deng, and Y. Zhao, “Coordination control between excitation and hydraulic system during mode conversion of variable speed pumped storage unit,” *IEEE Trans. Power Electron.*, vol. 36, no. 9, pp. 10171–10185, Sep. 2021.

[7] R. Tiwari, R. Nilsen, O. Mo, and A. Nysveen, “Control methods for operation of pumped storage plants with full-size back-to-back converter fed synchronous machines,” *IEEE Trans. Ind. Appl.*, vol. 59, no. 6, pp. 6792–6803, Nov./Dec. 2023.

[8] Y. Ma, D. Zhu, X. Zou, Y. Kang, and J. M. Guerrero, “Transient characteristics and quantitative analysis of electromotive force for DFIG-based wind turbines during grid faults,” *Chin. J. Elect. Eng.*, vol. 8, pp. 3–12, Jun. 2022.

[9] B. Tipo, J. Li, and B. Qin, “Fault ride through capability enhancement of doubly fed wind generator using hybrid protection circuits,” in *Proc. IEEE 8th Int. Conf. Adv. Power System Automat. Protection*, 2019, pp. 1200–1203.

[10] R. Wang, H. Song, L. Han, L. Yan, B. Wang, and P. Zhao, “Study on LVRT of DFIG wind power system based on crowbar protection circuit,” in *Proc. IEEE Student Conf. Elect. Mach. Syst.*, 2018, pp. 1–6.

[11] Z. Din, J. Zhang, Y. Zhu, Z. Xu, and A. El-Naggar, “Impact of grid impedance on LVRT performance of DFIG system with rotor crowbar technology,” *IEEE Access*, vol. 7, pp. 127999–128008, 2019.

[12] T. Zheng, Z. P. Wei, and Y. N. Chi, “Short-circuit current characteristics of doubly-fed induction generator wind turbines considering crowbar protection action time,” *Automat. Elect. Power Syst.*, vol. 38, no. 5, pp. 25–30, Mar. 2014.

[13] W. Xiong, X. D. Zou, and Q. J. Huang, “Transient characteristics and parameter design of doubly-fed induction generators based on crowbar protection,” *Automat. Elect. Power Syst.*, vol. 39, no. 11, pp. 117–125, Jun. 2015.

[14] L. B. Li and P. Zhang, “Low voltage ride through (LVRT) research of DFIG,” in *Proc. 25th Chin. Control Decis. Conf.*, 2013, pp. 2691–2695.

[15] Z. Din et al., “Low voltage and high voltage ride-through technologies for doubly fed induction generator system: Comprehensive review and future trends,” *IET Renewable Power Gener.*, vol. 15, no. 3, pp. 614–630, Jan. 2021.

[16] J. Chen, D. Wang, Z. Peng, L. Liu, and J. Duan, “Adaptive extended State observer based direct voltage sliding mode control of stand-alone DFIG-DC system,” in *Proc. 5th Int. Conf. Intell. Auton. Syst.*, 2022, pp. 303–308.

[17] I. Villanueva, A. Rosales, P. Ponce, and A. Molina, “Grid-voltage-oriented sliding mode control for DFIG under balanced and unbalanced grid faults,” *IEEE Trans. Sustain. Energy*, vol. 9, no. 3, pp. 1090–1098, Jul. 2018.

[18] Y. Ma, D. Zhu, J. Hu, R. Liu, X. Zou, and Y. Kang, “Optimized design of demagnetization control for DFIG-based wind turbines to enhance transient stability during weak grid faults,” *IEEE Trans. Power Electron.*, vol. 40, no. 1, pp. 76–81, Sep. 2024.

[19] D. Campos-Gaona, E. L. Moreno-Goytia, and O. Anaya-Lara., “Fault ride-through improvement of DFIG-WT by integrating a two-degrees-of-freedom internal model control,” *IEEE Trans. Ind. Electron.*, vol. 60, no. 3, pp. 1133–1145, Aug. 2013.

[20] G. Manohar, S. Venkateshwarlu, and A. JayaLaxmi, “An elite approach for enhancement of LVRT in doubly fed induction generator (DFIG)-based wind energy conversion system (WECS): A FAMSANFIS approach,” *Soft Comput.*, vol. 26, no. 21, pp. 11315–11337, Nov. 2022.

[21] Q. Huang, X. Zou, D. Zhu, and Y. Kang, “Scaled current tracking control for doubly fed induction generator to ride-through serious grid faults,” *IEEE Trans. Power Electron*, vol. 31, no. 3, pp. 2150–2165, May 2016.

[22] T. Zhang et al., “Improved continuous fault ride through control strategy of DFIG-based wind turbine during commutation failure in the LCC-HVDC transmission system,” *IEEE Trans. Power Electron*, vol. 36, no. 1, pp. 459–473, Jun. 2021.

[23] S. Yang, Y. Chen, L. Chang, Z. Xie, and X. Zhang, “Virtual inductance self-demagnetization based LVRT control strategy for doubly fed WTs,” in *Proc. IEEE Appl. Power Electron. Conf. Expo.*, 2015, pp. 2988–2992.

[24] Z. Din, J. Zhang, J. Zhao, and Y. Jiang, “Doubly fed induction generator with cascade converter for improving dynamic performances,” in *Proc. IEEE Energy Convers. Congr. Expo.*, 2018, pp. 2568–2575.

[25] Z. Din et al., “Realization of fault ride through for doubly fed induction generator system with cascade converter,” *Int. Trans. Elect. Energy Syst.*, vol. 31, no. 3, Jan. 2021, Art. no. 50.

[26] Z. Yu, S. Yutian, L. Jiahong, and H. Jinming, “Research on the low voltage fault of doubly-fed variable speed pumped storage,” in *Proc. IEEE 5th Int. Elect. Energy Conf.*, 2022, pp. 3934–3939.

[27] D. Zhu, Z. Wang, Y. Ma, J. Hu, X. Zou, and Y. Kang, “Hybrid LVRT control of doubly-fed variable speed pumped storage to shorten crowbar operational duration,” *IEEE Trans. Power Electron.*, vol. 39, no. 11, pp. 14192–14203, Nov. 2024.

[28] D. Zhu, X. Zou, L. Deng, Q. Huang, S. Zhou, and Y. Kang, “Inductance-emulating control for DFIG-based wind turbine to ride-through grid faults,” *IEEE Trans. Power Electron.*, vol. 32, no. 11, pp. 8514–8525, Nov. 2017.